Completely Decentralized Active Balancing Battery Management System

Damien F. Frost and David A. Howey, *Member, IEEE*

***Abstract*—The performance of a string of series-connected batteries is typically restricted by the worst cell in the string and a single failure point will render the entire string unusable. To address these issues, we present a decentralized battery management system with no communication requirement based on a modular multilevel converter topology with a distributed inductor and distributed controller running on a local microprocessor. This configuration is referred to as a "smart cell." By sensing the voltage across the local distributed inductor, each smart cell is able to: first, determine its optimal switching pattern in order to minimize the output voltage ripple; and second, adjust its duty cycle to synchronize its state of charge (SOC) with the average SOC of the series string of cells. The decentralized controller is derived using the theory of Kuramoto oscillators, and the stability of a system of smart cells is investigated. We experimentally show that a system of three smart cells with their decentralized controllers can accurately synchronize the SOC while minimizing their output voltage ripple.**

***Index Terms*—Batteries, battery chargers, distributed control, energy conversion, energy storage, power converter.**

I. Introduction

THE integration of power electronics into the interfaces of green energy technologies to the grid is playing a key role in the reduction of greenhouse gas emissions [1], [2]. In particular, electrical energy storage systems such as lithium-ion battery packs are seeing an increased penetration of power electronics [3], and the market for such devices is growing very rapidly as costs decrease [4]. Grid connected energy storage systems require state-of-the-art power electronics converters and energy management systems to ensure that the most expensive component of the energy storage system, the electrochemical battery pack [5], is operated in a safe and reliable manner [6], [7].

Alongside this, many companies who sell electric vehicles (EVs) and hybrid electric vehicles (HEVs) are investigating innovative ways to handle the influx of battery waste from these vehicles. The battery of an EV or HEV is considered to be at the end of its (first) life if its state of health (SOH), usually measured in terms of nominal capacity, falls to around 70%–80% of its original value [8], [9]. Although at this point the battery pack may be considered useless for portable applications, it still contains a lot of residual value for stationary energy storage applications [10], [11]. Recently, there have been announcements from Nissan [12], BMW [13], and GM [14], who are all experimenting with energy storage systems using batteries recovered from their EVs and HEVs.

For certain cell chemistries, individual cell monitoring is necessary. As an example, lithium-ion battery technology is unsafe if overcharged, where cells may explode or rupture [15], [16]. In the worst case scenario, an unmanaged series string of batteries will be limited by the weakest cell [17], thus a single failed cell can render the entire string useless. Therefore, in order to maximize the energy storage potential of several cells connected together in a pack, especially cells of varying capacities and usage histories, the state of charge (SOC) of individual cells in a battery pack must be measured and balanced. For enhanced performance, active cell balancing is chosen as the preferred method. Active cell balancing circuits fall within two main categories: energy reallocation and variable loading/charging. The most basic energy reallocation topology uses a switched capacitor system [18]–[20], however since the amount of charge moved from one cell to another is proportional to the difference in cell voltage, balancing times are slow especially as the cells become more balanced. In order to overcome some of the drawbacks of switched capacitor topologies, balancing circuits using a multiwinding flyback topology have also been proposed [21], [22]. In general, all energy reallocation topologies are only able to cope with a small mismatch is cell capacities, and therefore are not suitable in situations where cells have wildly varying capacities.

The drawbacks of balancing with energy reallocation can be overcome with active balancing by variable loading/charging. This can be accomplished by placing an individual power converter and battery management system (BMS) on every cell [23]–[25]. Although active cell management at the cell level is still an expensive option, recent advancements in wide bandgap switching devices, whose cost is expected to decrease over time, will increase conversion efficiencies (and reduce power losses), and reduce overall system costs through higher power density [26]–[28] and decreased cooling requirements [29].

We present work on a cell-level BMS and power converter, which uses a decentralized control strategy to regulate the SOC of serially connected cells of varying capacities. In the literature, there are examples of BMS's with global information and

Manuscript received September 22, 2016; revised November 29, 2016; accepted January 22, 2017. Date of publication February 6, 2017; date of current version October 6, 2017. This work was supported in part by the Newtons4th Ltd., in part by the Natural Sciences and Engineering Research Council of Canada, in part by the Jesus College Oxford, and in part by the John Fell Oxford University Press Research Fund. Recommended for publication by Associate Editor B. Semail.

The authors are with the Department of Engineering Science, University of Oxford, Oxford OX1 3PJ, U.K. (e-mail: damien.frost@eng.ox.ac.uk; david.howey@eng.ox.ac.uk).

Color versions of one or more of the figures in this paper are available online at http://ieeexplore.ieee.org.

Digital Object Identifier 10.1109/TPEL.2017.2664922

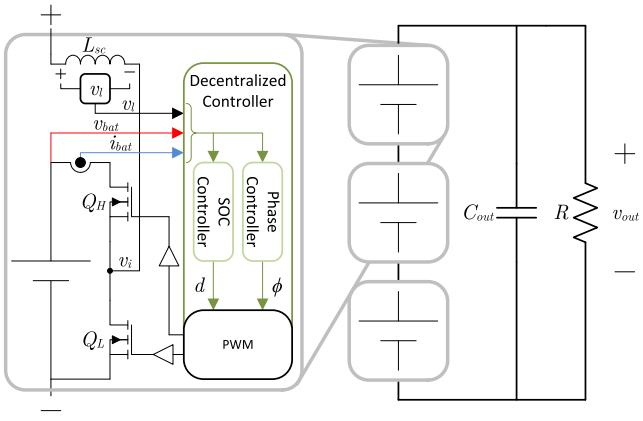

Fig. 1. Example of a system containing three "smart cells."

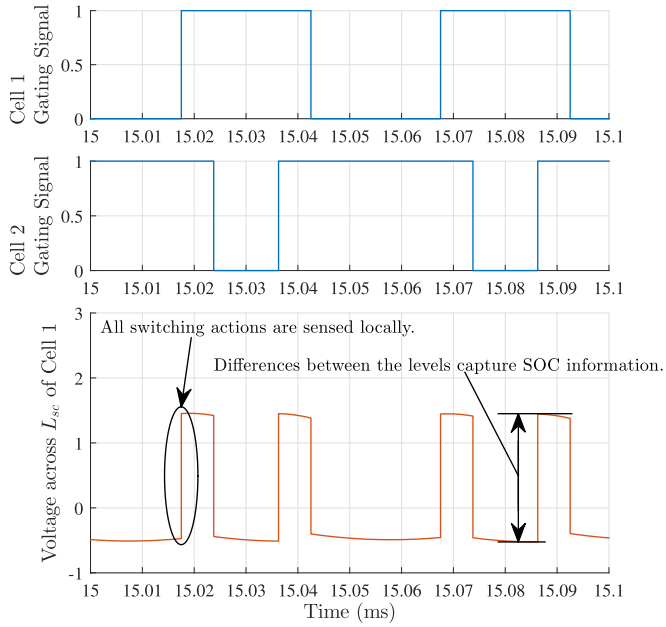

Fig. 2. Simulation of two smart cells switching, showing the voltage across the sensing inductor and its salient features.

control [30]–[32], systems with low-bandwidth communication [33], [34], or a sparse communication networks [35]–[35], and systems that use isolated cell-level converters connected to an auxiliary voltage bus implementing a droop controller [37], [38]. Conversely, this paper introduces a completely decentralized controller that *does not rely on any communication, or an auxiliary voltage bus*. The distributed BMS is designed to discharge and charge each cell in a series string of cells proportional to its capacity using a local converter that can actively balance its local cell with variable loading/charging. The converters are also controlled in such a way as to minimize the size of the filtering components in the series string.

II. System Architecture

An example of the proposed system architecture is shown in Fig. 1, and was first presented in [39]. In this example, the system is constructed out of three Modular Multilevel Converter (MMC) cells each containing a half-bridge switching network similar to the switching networks found in the submodules of MMC converters [40]. The MMC topology has already been used to integrate large battery packs for high-power applications [32], [41], however what we are proposing is to use the MMC in a low-power application. Each submodule, which we shall in this paper call a "smart cell," has the following two distinct features that make it different from a standard MMC submodule:

1) there exists an independent, decentralized controller in each smart cell;
2) each smart cell includes a small filter inductor, L_{sc}.

The decentralized controller manages the SOC, and monitors the SOH of its locally connected battery cell. This information is used to apply a duty cycle to the switches Q_L and Q_H, such that the connected battery cell discharges in proportion to its capacity. Discharging all cells in proportion to their respective capacities yields following two large benefits for the string of smart cells:

1) the SOC of all of the cells in the string will be synchronized;
2) larger, healthier battery cells will be loaded more than the smaller, more degraded battery cells; thus, the pack will degrade at a more uniform rate [42].

The voltage across the small filter inductor v_l contains all of the information required for each smart cell to determine its optimal switching pattern, and to adjust its duty cycle to synchronize its SOC with the other smart cells in the string. Fig. 2 is a simulation of a two smart cell system switching in its optimal switching pattern, with the voltage across one of the sense inductors shown. As shown in the figure, all of the switching transitions are captured by the sense inductor L_{sc}. Section III describes how the optimal switching pattern is obtained using the transitions of v_l, and Section IV describes how the phase controller of Fig. 1 is designed. Section VI describes how the SOC of the string is synchronized using the voltage across v_l, and the design of the SOC controller of Fig. 1.

In addition to sensing, L_{sc} is used as a distributed inductor to provide output filtering. Eventually L_{sc} could be small enough to be implemented on the trace of a printed circuit board (PCB), greatly reducing the cost and size of this component. The dc output to the load requires a small filter capacitor C_{out} whose capacitance depends on the application requirements.

III. Optimal Switching Pattern

In order to minimize the output voltage ripple measured at v_{out}, an optimal switching pattern of all of the switches Q_H and Q_L, of all of the smart cells, must be determined. This is done by all smart cells collectively minimizing the ac-rms inductor current. The full derivations of the results of this section were originally presented in [39].

Given a set of M battery cells with capacities $C = \{C_1, C_2, \ldots, C_M\}$, our objective is to find a set of phase timings, $\theta = \{\theta_1, \theta_2, \ldots, \theta_M\}$ for the turn-on of each smart cell, which will minimize the ripple current in the local inductor L_{sc}, thus minimizing the output ripple voltage. It is reasonable to assume that the nominal voltage of all of the battery cells is

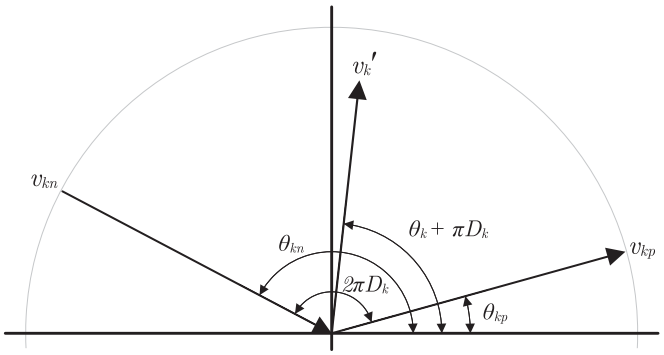

Fig. 3. Representing the switching action of the kth smart cell as a vector, with its weighted, phase shifted vector v_k'. The switching actions of the kth smart cell are also shown as vectors v_{kp} and v_{kn}.

$V_{\text{nom}} = V_1 = V_2 =, \ldots, = V_M$ since the SOC of all of the battery cells will be synchronized. The duty cycle of the ith smart cell can be calculated using the following equation:

$$D_i = \frac{C_i}{C_{\text{MAX}}} \tag{1}$$

where C_{MAX} is the maximum capacity expected within set C among all of the cells, such that $0 \leq D_i \leq 1$ for all i. Frost and Howey [39] show that an analytical expression for the ac-rms inductor current as a function of the smart cells' duty cycles and phase angles is

$$I^2_{\text{Lac-rms}} = \frac{1}{2}\left(\frac{V_{\text{nom}} T_s}{2\pi L}\right)^2 \sum_{n=1}^{\infty}\sum_{i=1}^{M}\sum_{j=1}^{M} \frac{4}{\pi^2 n^4} \left[\sin(\pi n D_i) \cdot \right.$$
$$\left. \sin(\pi n D_j)\cos\left(\pi n (D_i - D_j) + n(\theta_i - \theta_j)\right)\right]. \tag{2}$$

Equation (2) can be minimized to determine an optimal set $\theta = \{\theta_1, \theta_2, \ldots, \theta_M\}$ that will minimize the ac-rms current in the inductor L_{sc}, and therefore, the output voltage ripple in v_{out}.

A. Simplifying the Problem

Examining (2), we see that solving for an optimal set θ to minimize $I_{\text{Lac-rms}}$ is nontrivial, and difficult to achieve without significant computational power and global information about the system. Therefore, in this section, we present a way to identify a set θ, which will yield a satisfactory solution, with significantly less computational requirements, and in a decentralized fashion.

First, let us represent the switching action of the kth smart cell as a vector v_k in the unit circle as depicted in Fig. 3. The kth smart cell will turn ON at θ_k, and turn OFF at $\theta_k + 2\pi D_k$. Now, define a new vector, v_k' that will be known as the weighted vector, whose phase places the vector half way between the turn ON and turn OFF times and whose length is $\sin(\pi D_k)$. Therefore the phase and length of the weighted vector v_k' are given by

$$\angle v_k' = \theta_k' = \theta_k + \pi D_k \tag{3}$$
$$|v_k'| = \sin(\pi D_k). \tag{4}$$

Applying the transformation described in (3) and (4) to all of the smart cells, and summing all v_k', we can find the square of the magnitude of the total sum vector $|v_\Sigma'|^2$

$$|v_\Sigma'|^2 = \sum_{i=1}^{M}\sum_{j=1}^{M} \sin(\pi D_i)\sin(\pi D_j) \cdot$$
$$\cos\left(\pi(D_i - D_j) + \theta_i - \theta_j\right). \tag{5}$$

Equation (5) has the exact same form as (2) when $n = 1$ (i.e., only the fundamental is considered). Therefore, one control algorithm that will yield a suboptimal but acceptable minimum of (2) is to minimize the magnitude of the total sum vector $|v_\Sigma'|^2$.

B. Extracting Information From v_l

In order to minimize the magnitude of the total sum vector $|v_\Sigma'|^2$ found in (5), the duty cycle and phase shift of every smart cell in the string is still required. As shown in Fig. 2, every time a smart cell switches in and out of the string, this transition is captured by every sense inductor L_{sc} in the string of smart cells. Therefore, by observing when all of the positive and negative transitions occur in v_l, the "ON" and "OFF" times of all of the smart cells in the string can be determined. From this information, the phase shift and "ON" times of each cell in the string can be determined. The corresponding "OFF" time, and therefore duty cycle of each cell, cannot be uniquely determined.

However, as Frost and Howey have shown [39], there is no need to *pair* the correct "OFF" transition to its "ON" transition in order to minimize (5). Even if "ON" and "OFF" transitions are incorrectly paired together, the same minimum of (5) will be found.

IV. Phase Controller Design

The smart cell controller needs to be designed such that a group of cells working together will minimize (5). By taking the derivative of (5) and setting it to zero, the local minima can be found. The partial derivative of (5) with respect to θ_k is shown in the following equation:

$$\frac{\partial |v_\Sigma'|^2}{\partial \theta_k} = 2\sin(\pi D_k) \cdot$$
$$\sum_{i=1;i\neq k}^{M} \sin(\pi D_i)\sin\left(\pi(D_i - D_k) + \theta_i - \theta_k\right). \tag{6}$$

Graphically, setting (6) to zero is equivalent to "pointing" the weighted vector v_k' in either an opposite direction or the same direction, to all of the other weighted vectors $v_{i,i\neq k}'$ summed together. Clearly, by "pointing" v_k' in the same direction as $\sum_i v_{i,i\neq k}'$ would result in large currents in the inductor since all of the cells would eventually be in phase, maximizing the ripple current. However, if we chose to direct v_k' in the *opposite* direction to $\sum_i v_{i,i\neq k}'$, the current through the inductors will be reduced. Fig. 4 summarizes this observation.

Therefore, during each iteration of the smart cell controller, every smart cell will sum up the weighted vectors of all of the other smart cells it senses, and set its local reference to be 180° away from that sum. By doing this, each smart cell will be driving (6) to zero, thus finding a local minimum to (5). Using

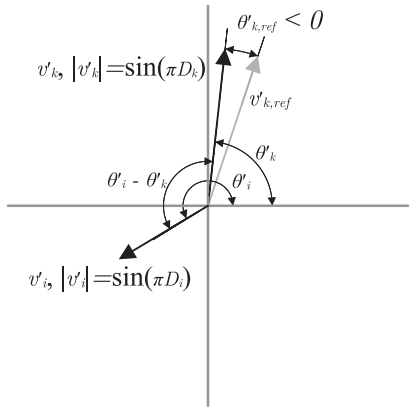

Fig. 4. Graphical representation of the weighted vectors v'_k and v'_i. By pointing these two vectors in the opposite direction, (5) will be minimized. This is accomplished with the controller of (7).

this controller design, (7) defines the reference angle $\theta'_{k,\text{ref}}$ for the kth smart cell's weighted sum vector v'_k

$$\theta'_{k,\text{ref}} = -2\sin(\pi D_k)\sum_{i=1;i\neq k}^{M}\sin(\pi D_i)\cdot \sin(\pi(D_i - D_k) + \theta_i - \theta_k). \tag{7}$$

Note the negative sign in (7), this ensures that that the angle between $\theta'_{k,\text{ref}}$ and $\sum_i v'_{i,i\neq k}$ is driven to π. Using (7) and the angle transformation of (3), a nonlinear model for the kth smart cell controller can be constructed, and is shown in the following equation:

$$\dot{\theta'_k} = \omega_k - 2\frac{K}{M}\sin(\pi D_k)\sum_{i=1;i\neq k}^{M}\sin(\pi D_i)\sin(\theta'_i - \theta'_k) \tag{8}$$

where ω_k is the switching frequency, and K is a controller constant.

V. Phase Controller Stability Analysis

Using the smart cell controller model developed in Section IV, the stability of a group of smart cells around local minima of (6) will be investigated. First, note that the controller chosen in (8) is very similar to the Kuramoto model of coupled oscillators [43], which is repeated in the following equation:

$$\dot{\theta_k} = \omega + \frac{K}{M}\sum_{i=1}^{N}\sin(\theta_i - \theta_k) \tag{9}$$

where ω is the nominal switching frequency of the system, M is the number of agents, and K is a global controller constant, identical for all agents.

First, consider the dynamics of the system described by (8) in a rotating reference frame, where all of the ω_k's are equal, thus $\omega_k = \omega$, and let

$$\theta'_k = \omega t + \gamma'_k. \tag{10}$$

Equation (8) becomes

$$\dot{\gamma'_k} = -2\frac{K}{M}\sin(\pi D_k)\sum_{i=1;i\neq k}^{M}\sin(\pi D_i)\sin(\gamma'_i - \gamma'_k) = f_k(\mathbf{\Gamma'}) \tag{11}$$

where $\mathbf{\Gamma'} = \{\gamma'_1, \gamma'_2, \ldots, \gamma'_M\}$. Linearize (11) around the equilibrium point $\mathbf{\Gamma'^\star} = \{\gamma^\star_1, \gamma^\star_2, \ldots, \gamma^\star_M\}$, to create the linear system defined by (12), which will be used to assess the stability of a group of smart cells around local minima of (5)

$$\dot{\mathbf{\Gamma'}} = -\frac{K}{M}\boldsymbol{L}\cdot\mathbf{\Gamma'} \tag{12}$$

where $\boldsymbol{L}$ is equivalent to the Jacobian matrix of (11) evaluated at the equilibrium point $\mathbf{\Gamma'^\star}$. Therefore, each element L_{ij} of the matrix $\boldsymbol{L}$ is defined explicitly as

$$L_{ij} = \begin{cases} -2\sin(\pi D_j)\sum_{i=1;i\neq j}^{M}\sin(\pi D_i)\cos\left(\gamma^\star_i - \gamma^\star_j\right), & i = j \\ 2\sin(\pi D_j)\sin(\pi D_i)\cos\left(\gamma^\star_i - \gamma^\star_j\right), & i \neq j. \end{cases} \tag{13}$$

The matrix $\boldsymbol{L}$ can also be represented by the partial derivatives of (5). Letting $\mathbf{\Theta^\star} = \{\theta^\star_1, \theta^\star_2, \cdots, \theta^\star_M\}$ be the corresponding equilibrium point of $\mathbf{\Gamma'^\star}$ yields

$$\boldsymbol{L} = \begin{bmatrix} \left.\frac{\partial^2|v'_\Sigma|^2}{\partial\theta_1^2}\right|_{\mathbf{\Theta^\star}} & \left.\frac{\partial^2|v'_\Sigma|^2}{\partial\theta_1\partial\theta_2}\right|_{\mathbf{\Theta^\star}} & \cdots & \left.\frac{\partial^2|v'_\Sigma|^2}{\partial\theta_1\partial\theta_M}\right|_{\mathbf{\Theta^\star}} \\ \left.\frac{\partial^2|v'_\Sigma|^2}{\partial\theta_2\partial\theta_1}\right|_{\mathbf{\Theta^\star}} & \left.\frac{\partial^2|v'_\Sigma|^2}{\partial\theta_2^2}\right|_{\mathbf{\Theta^\star}} & \cdots & \left.\frac{\partial^2|v'_\Sigma|^2}{\partial\theta_2\partial\theta_M}\right|_{\mathbf{\Theta^\star}} \\ \vdots & \vdots & \ddots & \vdots \\ \left.\frac{\partial^2|v'_\Sigma|^2}{\partial\theta_M\partial\theta_1}\right|_{\mathbf{\Theta^\star}} & \left.\frac{\partial^2|v'_\Sigma|^2}{\partial\theta_M\partial\theta_2}\right|_{\mathbf{\Theta^\star}} & \cdots & \left.\frac{\partial^2|v'_\Sigma|^2}{\partial\theta_M^2}\right|_{\mathbf{\Theta^\star}} \end{bmatrix}. \tag{14}$$

Equation (14) is simply the Hessian of the total sum vector $|v'_\Sigma|^2$ of (5) evaluated at $\mathbf{\Theta^\star}$. Since we chose $\mathbf{\Theta^\star}$ to be a local minimum of (5), we also know that (14) is positive semidefinite. Therefore, all of the eigenvalues of $-\boldsymbol{L}$ are all less than or equal to zero. As a consequence, the local minimum point $\mathbf{\Theta^\star}$ is an asymptotically attracting equilibrium point, and therefore a stable operating point.

It is not possible for $\boldsymbol{L}$ to be positive definite. This is due to the cyclic nature of oscillatory systems. For example, if $\mathbf{\Theta^\star}$ is a local minimum, then so is $\mathbf{\Theta^\star} + x$, where x is any angle. However, since we are only concerned about the relative angle between the smart cells to minimize (5), this is expected.

VI. SOC Controller Design

The SOC of each smart cell is regulated by synchronizing its SOC with the average SOC of a series string of smart cells, which is determined by analyzing v_l, the voltage across the sense inductor L_{sc}. The SOC controller relies on the string of smart cells being composed of cells of the same chemistry, so

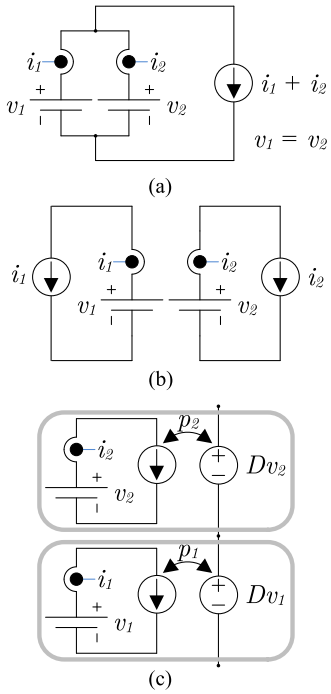

Fig. 5. Schematic showing the equivalence between the SOC controller of the smart cells and operation of the same cells in a parallel configuration.

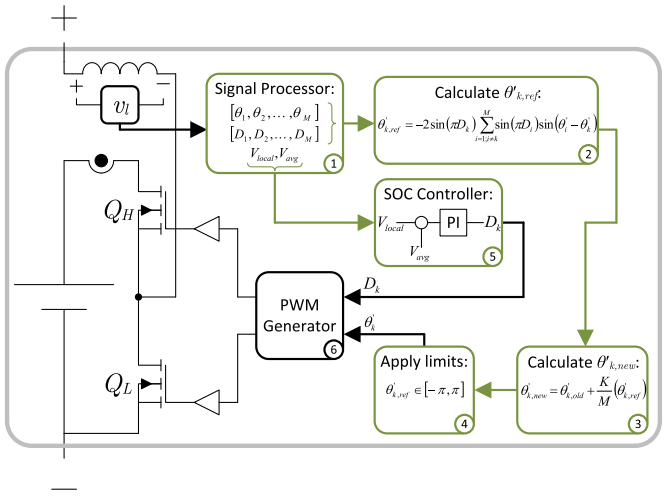

Fig. 6. Control block diagram of a smart cell built in MATLAB–Simulink. The steps 1–5 outlined in green are implemented in an embedded MATLAB function.

that there is a consistent relationship between the SOC and cell terminal voltage throughout the string.

As shown in Fig. 2, every time a smart cell switches in and out of the string, the voltage that it switches will be sensed by all of the sense inductors in the string of smart cells. Therefore, by calculating the differences in the levels of the v_l waveform, the terminal voltage of the cell that switched in or out can be extracted by each smart cell. Averaging all of these differences yields an average terminal voltage for the series string of smart cells. In order to account for variations in the inductance of L_{sc} and the sensing hardware, the gain of the v_l sensor is measured and adjusted every time the SOC controller is executed. Since the local cell knows its duty cycle and phase, it can determine which transitions in the v_l waveform are caused by its cell switching in and out of the circuit. Using these transitions, along with the local cell voltage measurement, the local cell can calculate the gain of its v_l sensor to correctly determine the voltages of the other cells switching in and out of the circuit.

The SOC controller adjusts the duty cycle of the local cell using a simple proportional-integral (PI) controller to synchronize its terminal voltage with the string's average terminal voltage. Operation in this manner is equivalent to operating the cells in parallel, as shown in the two cell example of Fig. 5. When two cells form a parallel pack of parallel cells, their terminal voltages are equal, and their output currents are i_1 and i_2, where i_1 is not necessarily the same as i_2, as shown in Fig. 5(a). One can split up this parallel connection, and load each cell individually with i_1 and i_2 such that their terminal voltages are *still* equal, as shown in Fig. 5(b). Thus, the two cells are operating as if they were connected in parallel. Finally, one can place the two cells in series, as shown in Fig. 5(c), operating them with currents i_1 and i_2, such that their terminal voltages are equal, and using a power converter to enable the series connection. The SOCs of parallel connected cells are considered to be nearly identical, and require no further management [44]. Thus, the SOC of series connected smart cells will also be well synchronized, without having to directly compute their SOC.

The one difference between the series connection of cells as shown in Fig. 5(c) and the parallel connection of cells as shown in Fig. 5(a) is that during rest (when there is no current flowing through the cells), the cell voltages will slowly return to their true open-circuit voltage. During this time, there may be current flowing between the parallel cells as each cell's internal chemical states reach their equilibrium. Although this would mean that the parallel cells would be perfectly balanced, this is not always necessarily advantageous, as there would be spurious current flowing during an "OFF" state, leading to ohmic losses and heat generation in the cells.

VII. Implementation of the Control Algorithm

A MATLAB–Simulink model of a smart cell using the theory developed in this paper was built using the SimPowerSystems toolbox. The model uses the Simscape battery model and MOSFETs to simulate the power circuit. The controller was implemented as an embedded MATLAB function, and is executed once per switching cycle when the upper MOSFET Q_H is switched ON.

Fig. 6 illustrates the algorithm the controller implements as a block diagram. Steps 1–5 are implemented by the embedded MATLAB function, which are as follows.

1) *Signal processor*: Detects all of the positive and negative transitions that occur during every switching cycle T_s. The local cell voltage V_{local} and the average cell voltage V_{avg} are measured using the levels of the v_l waveform. The edge detector also keeps track of the number of smart cells sensed in the string with a simple low-pass filter to average the number of smart cells.

TABLE I
PARAMETERS OF THE TWO SMART CELL SIMULATION STUDY

Description	Parameter	Value
Battery cell capacities	C_1	0.75 Ah
	C_2	1.20 Ah
	C_3	3.00 Ah
Smart cell parameters	L_{sc}	100 μH
	f_s	20 kHz
	V_{nom}	4.19 V
Output	C_{out}	54.7 μF
	R	4.8 Ω
Control parameters	K	10

2) *Calculate* $\theta'_{k,\text{ref}}$: A new reference phase shift is calculated using (7).
3) *Calculate* $\theta'_{k,\text{new}}$: The new phase that will be sent to the pulse width modulation (PWM) generator is calculated by the phase controller.
4) *Apply limits*: $\pm 2\pi$ is added to $\theta'_{k,\text{ref}}$ until it lies between $-\pi$ and π.
5) *SOC controller*: A new duty cycle is computed using V_{local} and V_{avg}. The updated duty cycle D_k is sent to the PWM module.
6) *PWM generator*: $\theta'_{k,\text{new}}$ is used by the PWM generator to produce gating signals for the MOSFETs.

The phase control loop, defined by steps 1–4 in Fig. 6, runs a hundred times faster than the SOC control loop. The SOC control loop is defined by steps 1 and 5, and will not modify the duty cycle unless the phase controller has reached a steady-state value.

The embedded MATLAB function that implements the controllers was converted into C++ code by MATLAB's coder toolbox for easy integration into the hardware.

VIII. SIMULATION STUDY OF THE PHASE CONTROLLER

A simulation study of a series string of three smart cells was undertaken to investigate the stability of the phase controller. Table I lists the simulation parameters used. The controller gain K was chosen through experimentation.

The simulation consists of the three smart cells operating completely independently of each other. The optimal switching controller is turned on 1.0 ms into the simulation. A value of $C_{\text{MAX}} = 4.00$ Ah was preprogrammed into each smart cell, in order for each smart cell to calculate its local duty cycle according to (1).

Fig. 7 shows how different characteristics of the system evolve over the length of the simulation. The smart cells initially all turn on at the same time, which produces a very high ac-rms ripple current in the inductor, as shown in the inset graphs. At the beginning of the simulation, $I_{\text{Lac-rms}}$ is 103 mA rms, and the peak-to-peak output voltage $v_{\text{out-pp}}$ is 43 mV. After the optimal switching controller is engaged, the phase shift of each smart cell gradually evolves smoothly into its steady-state value. At the end of the simulation, $I_{\text{Lac-rms}}$ and $v_{\text{out-pp}}$ have improved considerably to 26 mA rms and 6 mV, respectively.

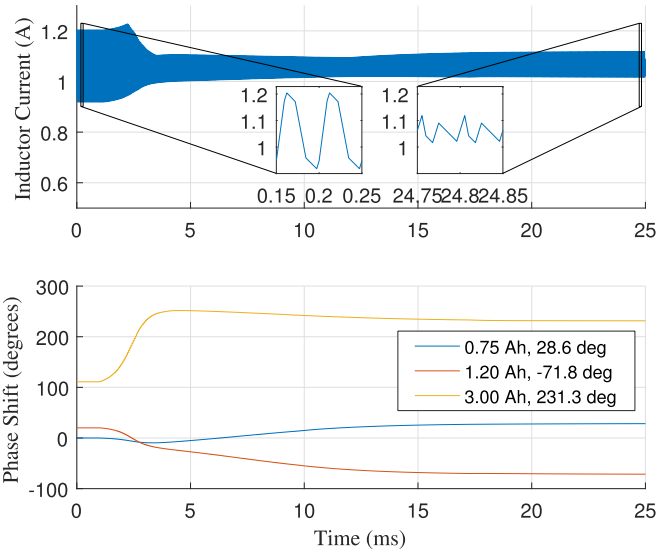

Fig. 7. Summary of the simulation results of a three smart cell pack. The smart cell controllers are turned on at 1.0 ms. The ac-rms current in the inductor is improved from 103 to 26 mA rms. Although not shown, the peak-to-peak ripple voltage on the capacitor is improved from 43 to 6 mV.

TABLE II
CELL CAPACITIES USED TO TEST THREE SMART CELL PCBS IN THE LABORATORY

Cell	Number of 18650 cells	Measured capacity
1	3	7.97 Ah
2	3	8.10 Ah
3	2	5.31 Ah

The amount of ripple current and ripple voltage reduction will depend heavily on duty cycles of the smart cells, thus a different group of smart cells may have less or more ripple reduction than shown here.

IX. EXPERIMENTAL RESULTS

A. Hardware Setup

The theory developed in this paper was tested in the laboratory with an experimental setup consisting of three smart cells in series, as shown in Fig. 1, using the parameters listed in Table I. The hardware was built around ARM's *mbed* platform, where each smart cell is implemented with the NUCLEO-F401RE board and a custom PCB containing the power stage. The inputs of each smart cell PCB was connected to a small pack of parallel connected 18650 lithium-ion cells, in order to simulate battery cells of varying capacities. Table II lists the capacities of the equivalent cell connected to each smart cell, as measured by a Neware battery tester, eight channel 5V20A-NTFA. The cells used were manufactured by Samsung, model number INR18650-29E [45]. The outputs of the smart cells were connected in series, and attached to a 4.8 Ω resistive load. Fig. 8 shows a photograph of the three smart cells built in the laboratory.

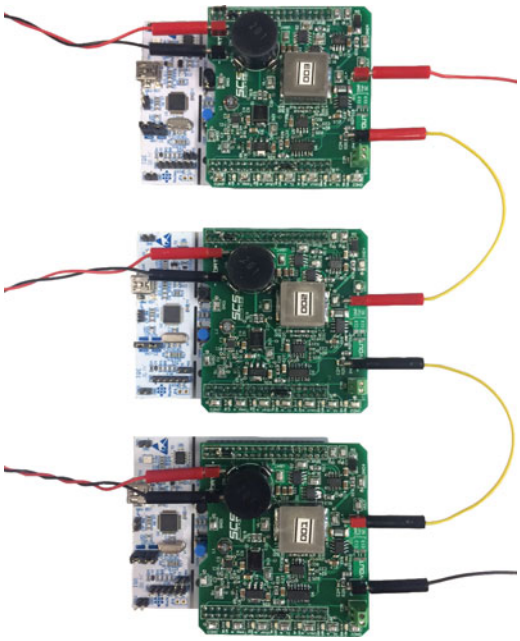

Fig. 8. Photograph of the three smart cell system operating in the laboratory. The battery cell connections are on the left, and the output is on the right. The smart cells were connected to a variety of cells.

The NUCLEO-F401RE board was chosen for its relatively powerful microcontroller, the STM32F401RET6, in order to focus attention on how the smart cell controller can be implemented in hardware. The STM32F401RET6 is based on the ARM 32-bit Cortex-M4 CPU and has a floating point unit. The analog-to-digital converter of the STM32F401RET6 was configured to its highest sample rate of 2.8 MHz while maintaining 12-b sampling resolution, to capture the details of the v_l waveform. The sampling rate and resolution of the Analog to Digital Converter (ADC) determine the accuracy of the phase controller and SOC controller, respectively. The ADC used in these experiments was able to detect changes in phase of 2.6°, and 3.6 mV change in terminal voltages. Using the same ADC, tighter phase regulation could be achieved by decreasing the switching frequency.

B. Phase Controller Performance

A first experiment using the preprogrammed capacities of Table I was carried out to verify the performance of the phase controller, whose role is to reduce the ac-rms current through the series string of smart cells.

Fig. 9 shows an oscilloscope screen shot of the four smart cells operating and finding their optimal switching pattern. The peak-to-peak voltage ripple from the experiments was reduced to 23 from 145 mV and the ac-rms $L_{\rm sc}$ ripple current was reduced to 25 from 95 mA. Note that the peak-to-peak value calculated by the oscilloscope, and shown in Fig. 9, includes some switching noise, which was ignored for the peak-to-peak output voltage measurements.

The smart cells operating in Fig. 9 settled to the same switching pattern as the simulated cells in Section VIII.

Fig. 9. Oscilloscope screen shot of the three smart cells operating at their optimal switching pattern, averaging applied with eight samples. Channel 2, top green trace, is the voltage across $L_{\rm sc}$ of the first smart cell with a capacity of C_1. Channel 2, middle blue trace, is the output voltage ripple. Channel 3, bottom pink trace, is the current in the smart cell inductors.

C. SOC Controller Performance

A second experiment to verify the performance of the SOC controller was also conducted. Each smart cell was connected to a fully charged set of cells, as listed in Table II. However, unlike the previous experiments and simulations, each smart cell started by operating with a duty cycle of 0.5. It became the role of the SOC controller to correct the mismatch in duty cycles to ensure all three smart cells discharged proportional to their capacity.

During operation, the SOC controller estimates the average string voltage by calculating the difference in levels as described in Section VI. Fig. 10 shows how the cell voltages and duty cycles evolved over time during the experiment.

As shown in Fig. 10, the duty cycles vary quite a bit during operation. This is due to the operation of the SOC controller, attempting to yield accurate voltage information from the string of switching smart cells. Since the controller relies on measuring the difference between levels to measure the average string voltage, there are moments during operation where these levels are nonexistent, for example, when all of the duty cycles sum to a positive integer. Therefore, to counteract this possibility, if a cell senses that it has not been able to measure the string voltage for more than 2.5 min, it increases or decreases its duty cycle by a fixed amount. This will introduce levels into the voltage measured across $L_{\rm sc}$, and the cells will be able to measure the average string waveform. This is exactly what is happening from about 75 to 200 min in the experimental results of Fig. 10. Cell 001 is modifying its duty cycle to get a better string measurement.

Due to the limited sampling resolution of the analog-to-digital converter, each cell implements a ± 10 mV dead zone [46] around its reference voltage.

At the end of the experiment, the cells were allowed to rest for 10 min, and their voltages were measured. The results are

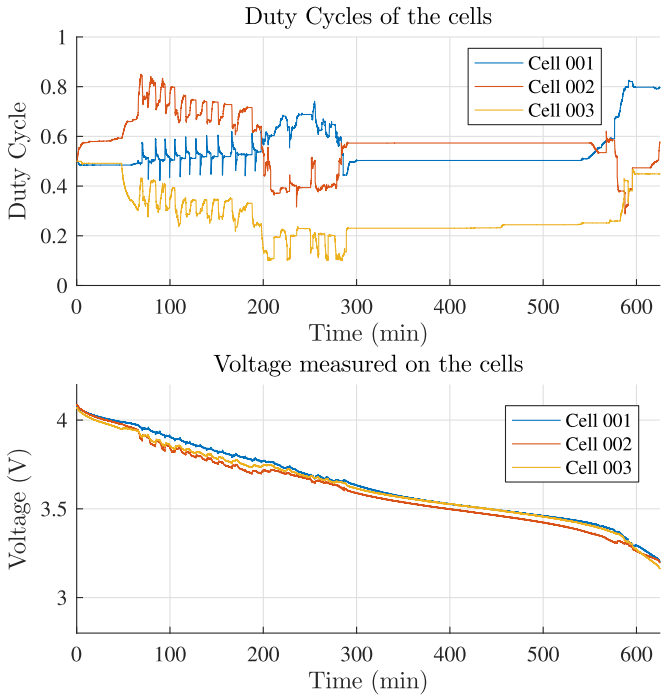

Fig. 10. Evolution of the duty cycles and cell voltages during the SOC controller test. "Steps" in the duty cycle are generated by the SOC controller when an average string voltage measurement cannot be obtained.

TABLE III
CELL VOLTAGES AT THE END OF THE SOC CONTROLLER EXPERIMENT AFTER 10 MIN OF REST

Cell	Voltage (V)
1	3.162
2	3.140
3	3.113

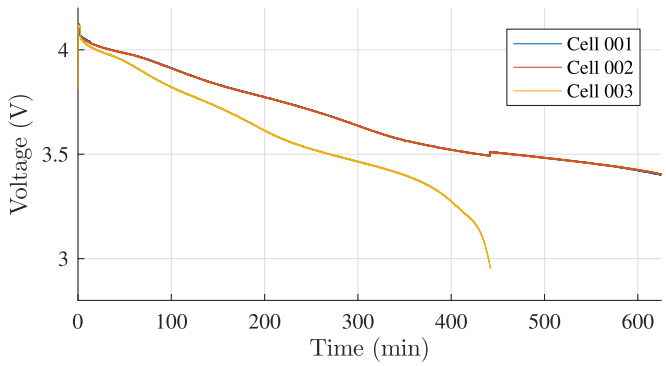

Fig. 11. Evolution of the cell voltages when the SOC controller is disabled, and a constant duty cycle of 0.5 is used by all cells.

shown in Table III, and they are all within 50 mV of each other. This is a very good result considering there is no communication between any of the smart cells. Furthermore, if the SOC controller was not operating, the string imbalance would have been much greater as shown in Fig. 11, where the smallest capacity cell discharges in around 450 min, clearly limiting the pack performance compared to the SOC controlled case.

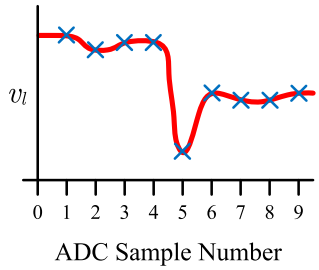

Fig. 12. Example of an ADC sampling a v_l waveform during a switching action with switching noise.

X. EXTENSION TO A LARGE NUMBER OF CELLS

In theory, the smart cell algorithms scale well with the number of cells, and are limited only by the sampling frequency of the ADC, as briefly mentioned in Section IX. An ADC that can sample quickly will be able to capture all of the salient features of the v_l waveform highlighted in Fig. 2, as required by the algorithm. Alternatively, if the ADC sampling rate is limited, the switching frequency of the smart cells could be decreased so that more samples of the v_l waveform can be captured every switching cycle.

For the system of three smart cells implemented in Section IX, the signal processor had to first identify the switching events by analyzing the output of the captured v_l waveform. The system was able to take 139 samples of v_l during the 20 kHz switching period. Fig. 12 is a drawing of what is recorded by the ADC during a switching event. As shown, there is a relatively constant value of v_l for samples 1–4, a cell switches just after sample number 4 with some switching noise as shown by the high value of $|dv_l/dt|$ between samples 4, 5, and 6, and then v_l settles down to its new steady-state value for samples 6–9. In order to accurately capture the switching events, the signal processor implemented a glitch filter to remove switching noise. The glitch filter ensured that there were no high $|dv_l/dt|$ events for at least one sample after an initial high $|dv_l/dt|$ event. Therefore using Fig. 12 as a guide, this would mean that the large $|dv_l/dt|$ event that occurred between samples 4 and 5 would be detected and recorded as a switching event, and the large $|dv_l/dt|$ event between samples 5 and 6 would be ignored.

Accurate cell terminal voltage measurements were achieved by averaging two samples before the switching event, and subtracting the average of the two samples after the switching event, ignoring the two samples around the switching event. Again using Fig. 12 as a guide, the higher voltage level would be calculated as the average of samples 2 and 3, and the lower voltage level would be calculated by averaging samples 6 and 7. Samples 4 and 5, which are around the switching event, are ignored.

In conclusion, to obtain accurate cell terminal voltage measurements, there should be at least four samples between each switching event. Therefore, keeping in mind that there are two switching events per cell, the smart cell system of Section IX is theoretically capable of operating with up to $\lfloor 139/4/2 \rfloor = 17$ smart cells in series.

Computationally, the smart cell algorithm also scales well with the number of cells. The most computationally demanding

part of the algorithm is the signal processor, depicted in Fig. 6, which scales linearly with the number of ADC samples. The SOC controller needs only to average the terminal voltage measurements from the signal processor, a simple operation that scales linearly with the number of cells. The phase controller calculates the reference angle using (7), a relatively simple operation, which also scales linearly with the number of cells.

Finally, as the number of smart cells increase, the voltage across each distributed inductor will decrease, leading to difficulties in sensing voltage levels. The accuracy of the voltage balancing is related to the resolution of the ADC, and the gain of the v_l sensor. To overcome this, smart cells could implement the v_l sensor with a variable gain to ensure that they capture all of the information. Since the gain of this sensor is recalibrated after every measurement, the variable gain can be implemented in a simple, low cost approach with a resistor array.

XI. Conclusion and Future Work

A completely decentralized BMS has been introduced based around the concept of a smart cell. The smart cell was built around: 1) a phase controller, which synchronized all of the switching actions of the cells to minimize the output voltage ripple, and 2) a SOC controller, which adjusted the duty cycle of the local smart cell to synchronize the local cell's voltage with the pack voltage, and thus, its SOC. This paper had particular focus on the phase controller: its design and stability. A system of smart cells was shown to be stable around local minima of (5). A practical BMS could be built around the theory of smart cells by adding a visual indicator to each cell indicating whether or not it has failed, and implementing a complete BMS at the cell level. In this scenario, a central monitoring function is not required and cells could be easily identified for replacement by a user. If high-level control of several cells is desired, a low cost, low power, and low bandwidth communication system could be added to provide additional pack benefits.

A novel way of augmenting the role of passive filtering components has also been introduced. Typically, power electronic designs measure the current through inductors and the voltage across capacitors to yield the current and voltage states of a system, respectively. In this paper, the voltage across the filtering inductor was measured to yield the switching states, and the average SOC of the system. Augmenting the role of passives has applications across all areas of power electronics, and could yield new methods of sensing and control. For example, one could measure the voltage across the filtering inductor of a buck or boost converter to yield both the input and output voltages with a single sensor. In another example, this work could be extended to use the voltage across v_l as part of a decentralized MMC controller for grid applications.

As presented, the smart cell concept has been shown to operate at the cell level. However, the same decentralized controller can be employed at higher power levels to break a series string of battery cells into packs instead of individual cells.

Future work on the smart cell will include the implementation of a complete BMS at the cell level, where the SOH and SOC will be managed by the decentralized controller. In particular, the SOC controller will be augmented with a battery model to improve its performance.

Fig. 13. Oscilloscope screen shot of the three smart cells operating with synchronized switching, averaging applied with eight samples. Channel 2, top green trace, is the voltage across $L_{\rm sc}$ of the first smart cell with a capacity of C_1. Channel 2, middle blue trace, is the output voltage ripple. Channel 3, bottom pink trace, is the current in the smart cell inductors.

Finally, some of the phase synchronization work presented here can be used to create completely decentralized MMC converters. Using a simple modification of multiplying (7) by -1, the smart cells can be designed in synchronization with their switching actions to produce sinusoidal output waveforms as depicted in Fig. 13.

References

[1] B. Bose, "Global warming: Energy, environmental pollution, and the impact of power electronics," *IEEE Ind. Electron. Mag.*, vol. 4, no. 1, pp. 6–17, Mar. 2010.

[2] B. Bose, "Power electronics and motor drives recent progress and perspective," *IEEE Trans. Ind. Electron.*, vol. 56, no. 2, pp. 581–588, Feb. 2009.

[3] S. Vazquez, S. Lukic, E. Galvan, L. Franquelo, and J. Carrasco, "Energy storage systems for transport and grid applications," *IEEE Trans. Ind. Electron*, vol. 57, no. 12, pp. 3881–3895, Dec. 2010.

[4] S. Wilkinson, "The grid-connected energy storage market is set to explode, reaching a total of over 40 GW of installations by 2022," IHS Technology, Jan. 15, 2014. [Online]. Available: https://technology.ihs.com/483008/the-grid-connected-energy-storage-market-is-set-to-explode-reaching-a-total-of-over-40-gw-of-installations-by-2022

[5] H. Chen, T. N. Cong, W. Yang, C. Tan, Y. Li, and Y. Ding, "Progress in electrical energy storage system: A critical review," *Progress Natural Sci.*, vol. 19, no. 3, pp. 291–312, 2009. [Online]. Available: http://www.sciencedirect.com/science/article/pii/S100200710800381X

[6] D. Andrea, *Battery Management Systems for Large Lithium-Ion Battery Packs*. Norwood, MA, USA: Artech House, Oct. 2010.

[7] J. Kimball, B. Kuhn, and P. Krein, "Increased performance of battery packs by active equalization," in *Proc. IEEE Veh. Power Propulsion Conf.*, Sep. 2007, pp. 323–327.

[8] D. Strickland, L. Chittock, D. Stone, M. Foster, and B. Price, "Estimation of transportation battery second life for use in electricity grid systems," *IEEE Trans. Sustain. Energy*, vol. 5, no. 3, pp. 795–803, Jul. 2014.

[9] C. Zhou, K. Qian, M. Allan, and W. Zhou, "Modeling of the cost of EV battery wear due to V2G application in power systems," *IEEE Trans. Energy Convers.*, vol. 26, no. 4, pp. 1041–1050, Dec. 2011.

[10] J. Neubauer and A. Pesaran, "The ability of battery second use strategies to impact plug-in electric vehicle prices and serve utility energy storage applications," *J. Power Sources*, vol. 196, no. 23, pp. 10351–10358, 2011. [Online]. Available: http://www.sciencedirect.com/science/article/pii/S0378775311012377

[11] L. Wen-Chen, J.-H. Yen, F.-H. Shieh, and Y.-M. Liao, "Second use of retired lithium-ion battery packs from electric vehicles: Technological challenges, cost analysis and optimal business model," in *Proc. 2012 Int. Symp. Comput., Consumer Control.*, Jun. 2012, pp. 381–384.
[12] P. Bennett, "Nissan to recycle electric vehicle batteries for commercial energy storage products," Clean Energy News, Jun. 2015. [Online]. Available: http://www.cleanenergynews.co.uk/news/storage/nissan-to-recycle-electric-vehicle-batteries-for-commercial-energy-storage
[13] P. Kelly-Detwiler, "BMW's i3: A new kind of electric vehicle," Forbes Energy, Jan. 2014. [Online]. Available: http://www.forbes.com/sites/peterdetwiler/2014/01/29/bmws-i3-a-new-kind-of-electric-vehicle/#53035c3c5996
[14] "GM, ABB demonstrate Chevrolet volt battery reuse unit," General Motors, Nov. 2012. [Online]. Available: http://media.gm.com/media/us/en/gm/news.detail.html/content/Pages/news/us/en/2012/Nov/electrification/1114_reuse.html
[15] R. A. Leising, M. J. Palazzo, E. S. Takeuchi, and K. J. Takeuchi, "Abuse testing of lithium-ion batteries: Characterization of the overcharge reaction of $LiCoO_2$/graphite cells," *J. Electrochem. Soc.*, vol. 148, no. 8, pp. A838–A844, 2001.
[16] L. Lu, X. Han, J. Li, J. Hua, and M. Ouyang, "A review on the key issues for lithium-ion battery management in electric vehicles," *J. Power Sources*, vol. 226, pp. 272–288, 2013. [Online]. Available: http://www.sciencedirect.com/science/article/pii/S0378775312016163
[17] J. Zhang, S. Ci, H. Sharif, and M. Alahmad, "Modeling discharge behavior of multicell battery," *IEEE Trans. Energy Convers.*, vol. 25, no. 4, pp. 1133–1141, Dec. 2010.
[18] C. Pascual and P. Krein, "Switched capacitor system for automatic series battery equalization," in *Proc. 12th Annu. Appl. Power Electron. Conf. Expo.*, Feb. 1997, vol. 2, pp. 848–854.
[19] S. W. Moore and P. J. Schneider, "A review of cell equalization methods for lithium ion and lithium polymer battery systems," SAE, Warrendale, PA, USA, Tech. Rep., Mar. 2001, doi:10.4271/2001-01-0959.
[20] H.-S. Park, C.-E. Kim, C.-H. Kim, G.-W. Moon, and J.-H. Lee, "A modularized charge equalizer for an HEV lithium-ion battery string," *IEEE Trans. Ind. Electron.*, vol. 56, no. 5, pp. 1464–1476, May 2009.
[21] M. Einhorn, W. Roessler, and J. Fleig, "Improved performance of serially connected Li-ion batteries with active cell balancing in electric vehicles," *IEEE Trans. Veh. Technol.*, vol. 60, no. 6, pp. 2448–2457, Jul. 2011.
[22] M. Einhorn *et al.*, "A current equalization method for serially connected battery cells using a single power converter for each cell," *IEEE Trans. Veh. Technol.*, vol. 60, no. 9, pp. 4227–4237, Nov. 2011.
[23] P. Weicker, *A Systems Approach to Lithium-Ion Battery Management*. Norwood, MA, USA: Artech House, Oct. 2013.
[24] C. R. Birkl and D. F. Frost and A. M. Bizeray and R. R. Richardson and D. A. Howey, "Modular converter system for low-cost off-grid energy storage using second life Li-ion batteries," in *Proc. IEEE Global Humanitarian Technol. Conf.*, Oct. 2014, pp. 192–199.
[25] H. Qian, J. Zhang, J.-S. Lai, and W. Yu, "A high-efficiency grid-tie battery energy storage system," *IEEE Trans. Power Electron.*, vol. 26, no. 3, pp. 886–896, Mar. 2011.
[26] M. Rodriguez, Y. Zhang, and D. Maksimovic, "High-frequency PWM buck converters using GaN-on-SiC HEMTs," *IEEE Trans. Power Electron.*, vol. 29, no. 5, pp. 2462–2473, May 2014.
[27] D. Reusch, D. Gilham, Y. Su, and F. Lee, "Gallium nitride based 3d integrated non-isolated point of load module," in *Proc. 2012 27th Annu. IEEE Appl. Power Electron. Conf. Expo.*, Feb. 2012, pp. 38–45.
[28] T. McDonald, "GaN based power technology stimulates revolution in conversion electronics," in *Electronics in Motion and Conversion*, Katzbek 17a D-24235 Laboe: BODO's Power System, 2009, pp. 2–4.
[29] J. Millan, P. Godignon, X. Perpina, A. Perez-Tomas, and J. Rebollo, "A survey of wide bandgap power semiconductor devices," *IEEE Trans. Power Electron.*, vol. 29, no. 5, pp. 2155–2163, May 2014.
[30] T. Kim, W. Qiao, and L. Qu, "Power electronics-enabled self-X multicell batteries: A design toward smart batteries," *IEEE Trans. Power Electron.*, vol. 27, no. 11, pp. 4723–4733, Nov. 2012.
[31] L. Tan, B. Wu, S. Rivera, and V. Yaramasu, "Comprehensive dc power balance management in high-power three-level dc-dc converter for electric vehicle fast charging," *IEEE Trans. Power Electron.*, vol. 31, no. 1, pp. 89–100, Jan. 2016.
[32] L. Maharjan, T. Yamagishi, and H. Akagi, "Active-power control of individual converter cells for a battery energy storage system based on a multilevel cascade PWM converter," *IEEE Trans. Power Electron.*, vol. 27, no. 3, pp. 1099–1107, Mar. 2012.
[33] K. Cermak and M. Bartl, "Decentralized battery management system," in *Proc. 2014 15th Int. Sci. Conf. Elect. Power Eng.*, May 2014, pp. 599–603.
[34] Y. Li and Y. Han, "A module-integrated distributed battery energy storage and management system," *IEEE Trans. Power Electron.*, vol. 31, no. 12, pp. 8260–8270, Dec. 2016.
[35] T. Morstyn, M. Momayyezan, B. Hredzak, and V. Agelidis, "Distributed control for state of charge balancing between the modules of a reconfigurable battery energy storage system," *IEEE Trans. Power Electron.*, vol. 31, no. 11, pp. 7986–7995, Nov. 2016.
[36] S. Abhinav, G. Binetti, A. Davoudi, and F. Lewis, "Toward consensus-based balancing of smart batteries," in *Proc. 2014 29th Annu. IEEE Appl. Power Electron. Conf. Expo.*, Mar. 2014, pp. 2867–2873.
[37] M. M. U. Rehman, F. Zhang, M. Evzelman, R. Zane, and D. Maksimovic, "Control of a series-input, parallel-output cell balancing system for electric vehicle battery packs," in *Proc. 2015 IEEE 16th Workshop Control Model. Power Electron.*, Jul. 2015, pp. 1–7.
[38] F. Zhang *et al.*, "State-of-charge estimation based on microcontroller-implemented sigma-point Kalman filter in a modular cell balancing system for lithium-ion battery packs," in *Proc. 2015 IEEE 16th Workshop Control Model. Power Electron.*, Jul. 2015, pp. 1–7.
[39] D. Frost and D. Howey, "Novel MMC control for active balancing and minimum ripple current in series-connected battery strings," in *Proc. 2015 17th Eur. Conf. Power Electron. Appl.*, Sep. 2015, pp. 1–10.
[40] A. Lesnicar and R. Marquardt, "An innovative modular multilevel converter topology suitable for a wide power range," in *Proc. 2003 IEEE Bologna Power Tech Conf. Proc.*, Jun. 2003, vol. 3, pp. 6–11.
[41] J. Ota, T. Sato, and H. Akagi, "Enhancement of performance, availability, and flexibility of a battery energy storage system based on a modular multilevel cascaded converter (MMCC-SSBC)," *IEEE Trans. Power Electron.*, vol. 31, no. 4, pp. 2791–2799, Apr. 2016.
[42] S. S. Choi and H. S. Lim, "Factors that affect cycle-life and possible degradation mechanisms of a Li-ion cell based on $LiCoO_2$," *J. Power Sources*, vol. 111, no. 1, pp. 130–136, 2002. [Online]. Available: http://www.sciencedirect.com/science/article/pii/S0378775302003051
[43] Y. Kuramoto and H. Araki, "Lecture notes in physics, " in, *International Symposium on Mathematical Problems in Theoretical Physics*. New York, NY, USA: Springer, 1975.
[44] L. Zhong, C. Zhang, Y. He, and Z. Chen, "A method for the estimation of the battery pack state of charge based on in-pack cells uniformity analysis," *Appl. Energy*, vol. 113, pp. 558–564, 2014. [Online]. Available: http://www.sciencedirect.com/science/article/pii/S0306261913006430
[45] Samsung INR18650-29E Datasheet, Sep. 2012.
[46] A. Prodic, D. Maksimovic, and R. Erickson, "Dead-zone digital controllers for improved dynamic response of low harmonic rectifiers," *IEEE Trans. Power Electron.*, vol. 21, no. 1, pp. 173–181, Jan. 2006.

Damien Francis Frost received the B.A.Sc. degree in Engineering Science and M.A.Sc. degree Power Electronics from the University of Toronto, Toronto, ON, Canada, in 2007 and 2009, respectively. Since 2013, he has been working toward the D.Phil (Ph.D.) degree in the Energy and Power Group, Department of Engineering Science, University of Oxford, Oxford, U.K., and is currently in his fourth year.

Before 2013, he was in the solar industry as a cofounder and Power Electronics Designer in the ARDA Power. His current research focuses on the application of power electronics and control theory to battery management systems.

David A. Howey (M'10) received the B.A. and M.Eng. degrees in Electrical and Information Sciences from the University of Cambridge, Cambridge, U.K., in 2002, and the Ph.D. degree in Electrical Engineering from Imperial College London, London, U.K., in 2010.

He is currently an Associate Professor in the Energy and Power Group, Department of Engineering Science, University of Oxford, Oxford, U.K. He leads projects on fast electrochemical modeling, model-based battery management systems, battery thermal management, and motor degradation. His research interests include condition monitoring and management of electric and hybrid vehicle components.